membrane-buried isoprenyl moiety of Rac1, removes GDP-bound Rac1 from the membrane (Fig. 3A). On the other hand, ΔC-RhoGDIβ binds GTP-bound Rac1 by the N-terminal regulatory domain but can not remove Rac1 from the membrane due to the defective isoprenyl-binding pocket, therefore ΔC-RhoGDIβ keeps GTP-bound Rac1 on the membrane and supports Rac1 activation of the effectors (Fig. 3B).

The expression level of RhoGDIs is correlated to cancer progression, both positively (Tapper et al., 2001; Fritz et al., 2002; Jones et al., 2002; Yanagawa et al., 2004) and negatively (Seraj et al., 2000; Gildea et al., 2002; Jiang et al., 2003). RhoGDIs are often thought to function as inhibitors, however, we had shown that RhoGDIβ could positively regulate Rac1 (Ota et al., 2004). Several other studies also suggest a positive regulatory role for RhoGDIs (O'Sullivan et al., 1996; Tolias et al., 1998). Our observations in this report suggest that the interaction of RhoGDIβ with the isoprenyl moiety of Rac1 is a crucial determinant of the nature of regulatory functions of RhoGDIβ. The apparently opposite roles of RhoGDIs in cancer progression may reflect different regulation mechanisms of Rho GTPases by RhoGDIs mediated by interaction of RhoGDIs with the isoprenyl moiety of Rho GTPases.

Acknowledgements

This research was supported in part by Grants-in-Aid for Scientific Research from the Japan Society for the Promotion of Science, Project Research from High Technology Center (H2006-8), Grant for Collaborative Research (C2005-2) of Kanazawa Medical University, the Science Research Promotion Fund of The Promotion and Mutual Aid Corporation for Private Schools of Japan and by the Two Cell Co. Ltd.

References

Chuang TH, Xu X, Knaus UG, Hart MJ, Bokoch GM. GDP dissociation inhibitor prevents intrinsic and GTPase activating protein-stimulated GTP hydrolysis by the Rac GTP-binding protein. J Biol Chem 1993;268:775–8.

Etienne-Manneville S, Hall A. Rho GTPases in cell biology. Nature 2002; 420:629–35.

Faure J, Dagher M. Interactions between Rho GTPases and Rho GDP dissociation inhibitor (Rho-GDI). Biochimie 2001;83:409–14.

Fritz G, Brachetti C, Bahlmann F, Schmidt M, Kaina B. Rho GTPases in human breast tumours: expression and mutation analyses and correlation with clinical parameters. Br J Cancer 2002;87:635–44.

Gildea JJ, Seraj MJ, Oxford G, Harding MA, Hampton GM, Moskaluk CA, et al. RhoGDI2 is an invasion and metastasis suppressor gene in human cancer. Cancer Res 2002;62:6418–23.

Gosser YQ, Nomanbhoy TK, Aghazadeh B, Manor D, Combs C, Cerione RA, et al. C-terminal binding domain of Rho GDP-dissociation inhibitor directs N-terminal inhibitory peptide to GTPases. Nature 1997;387:814–9.

Grizot S, Faure J, Fieschi F, Vignais PV, Dagher MC, Pebay-Peyroula E. Crystal structure of the Rac1-RhoGDI complex involved in nadph oxidase activation. Biochemistry 2001;40:10007–13.

Hoffman GR, Nassar N, Cerione RA. Structure of the Rho family GTP-binding protein Cdc42 in complex with the multifunctional regulator RhoGDI. Cell 2000;100:345–56.

Hori Y, Kikuchi A, Isomura M, Katayama M, Miura Y, Fujioka H, et al. Post-translational modifications of the C-terminal region of the rho protein are important for its interaction with membranes and the stimulatory and inhibitory GDP/GTP exchange proteins. Oncogene 1991;6: 515–22.

Jiang WG, Watkins G, Lane J, Cunnick GH, Douglas-Jones A, Mokbel K, et al. Prognostic value of rho GTPases and rho guanine nucleotide dissociation inhibitors in human breast cancers. Clin Cancer Res 2003;9: 6432–40.

Jones MB, Krutzsch H, Shu H, Zhao Y, Liotta LA, Kohn EC, et al. Proteomic analysis and identification of new biomarkers and therapeutic targets for invasive ovarian cancer. Proteomics 2002;2:76–84.

Lian LY, Barsukov I, Golovanov AP, Hawkins DI, Badii R, Sze KH, et al. Mapping the binding site for the GTP-binding protein Rac-1 on its inhibitor RhoGDI-1. Structure Fold Des 2000;8:47–55.

Michaelson D, Silletti J, Murphy G, D'Eustachio P, Rush M, Philips MR. Differential localization of Rho GTPases in live cells: regulation by hypervariable regions and RhoGDI binding. J Cell Biol 2001;152:111–26.

Moissoglu K, Slepchenko BM, Meller N, Horwitz AF, Schwartz MA. In vivo dynamics of Rac-membrane interactions. Mol Biol Cell 2006;17: 2770–9.

Nomanbhoy TK, Erickson JW, Cerione RA. Kinetics of Cdc42 membrane extraction by Rho-GDI monitored by real-time fluorescence resonance energy transfer. Biochemistry 1999;38:1744–50.

O'Sullivan AJ, Brown AM, Freeman HN, Gomperts BD. Purification and identification of FOAD-II, a cytosolic protein that regulates secretion in streptolysin-O permeabilized mast cells, as a rac/rhoGDI complex. Mol Biol Cell 1996;7:397–408.

Ota T, Maeda M, Suto S, Tatsuka M. LyGDI functions in cancer metastasis by anchoring Rho proteins to the cell membrane. Mol Carcinog 2004; 39:206–20.

Regazzi R, Kikuchi A, Takai Y, Wollheim CB. The small GTP-binding proteins in the cytosol of insulin-secreting cells are complexed to GDP dissociation inhibitor proteins. J Biol Chem 1992;267:17512–9.

Sasaki T, Kato M, Takai Y. Consequences of weak interaction of rho GDI with the GTP-bound forms of rho p21 and rac p21. J Biol Chem 1993;268: 23959–63.

Seraj MJ, Harding MA, Gildea JJ, Welch DR, Theodorescu D. The relationship of BRMS1 and RhoGDI2 gene expression to metastatic potential in lineage related human bladder cancer cell lines. Clin Exp Metastasis 2000;18:519–25.

Sun J, Barbieri JT. ExoS Rho GTPase-activating protein activity stimulates reorganization of the actin cytoskeleton through Rho GTPase guanine nucleotide disassociation inhibitor. J Biol Chem 2004;279:42936–44.

Tapper J, Kettunen E, El-Rifai W, Seppala M, Andersson LC, Knuutila S. Changes in gene expression during progression of ovarian carcinoma. Cancer Genet Cytogenet 2001;128:1–6.

Tatsuka M, Ota T, Yamagishi N, Kashihara Y, Wada M, Matsuda N, et al. Different metastatic potentials of ras- and src-transformed BALB/c 3T3 A31 variant cells. Mol Carcinog 1996;15:300–8.

Tatsuka M, Ota T, Maeda M, Wada M, Yamagishi N, Taniguchi S, et al. A BALB/c 3T3-transformed cell line suitable for transfection assay of metastasis-inducing genes. Int J Cancer 1997;71:88–93.

Thapar R, Karnoub AE, Campbell SL. Structural and biophysical insights into the role of the insert region in Rac1 function. Biochemistry 2002;41: 3875–83.

Tolias KF, Couvillon AD, Cantley LC, Carpenter CL. Characterization of a Rac1- and RhoGDI-associated lipid kinase signaling complex. Mol Cell Biol 1998;18:762–70.

Wennerberg K, Der CJ. Rho-family GTPases: it's not only Rac and Rho (and I like it). J Cell Sci 2004;117:1301–12.

Yanagawa T, Watanabe H, Takeuchi T, Fujimoto S, Kurihara H, Takagishi K. Overexpression of autocrine motility factor in metastatic tumor cells: possible association with augmented expression of KIF3A and GDI-beta. Lab Invest 2004;84:513–22.

Skeletal Radiol (2006) 35: 27 33
DOI 10.1007/s00256-005-0021-0

SCIENTIFIC ARTICLE

Ukihide Tateishi
Tadashi Hasegawa
Takayuki Nojima
Tsutomu Takegami
Yasuaki Arai

MRI features of extraskeletal myxoid chondrosarcoma

Received: 23 February 2005
Revised: 13 May 2005
Accepted: 27 July 2005

All authors of this research paper have directly participated in the planning, execution, or analysis of the study
The contents of this manuscript have not been copyrighted or previously published
There are no directly related manuscripts or abstracts, published or unpublished, by any authors of this paper

U. Tateishi (✉) · Y. Arai
Division of Diagnostic Radiology,
National Cancer Center Hospital,
5-1-1, Tsukiji, Chuo-Ku,
104-0045 Tokyo, Japan
e-mail: utateish@ncc.go.jp
Tel.: +81-3-35422511
Fax: +81-3-35423815

T. Hasegawa
Department of Clinical Pathology,
Sapporo Medical University
School of Medicine,
Sapporo, Japan

T. Nojima
Department of Pathology,
Kanazawa Medical University,
Ishikawa, Japan

T. Takegami
Division of Molecular Oncology
and Virology,
Medical Research Institute,
Kanazawa Medical University,
Ishikawa, Japan

Abstract *Objective:* To describe the MRI features of extraskeletal myxoid chondrosarcoma in comparison with clinicopathologic findings. *Design and patients:* The study comprised 12 male subjects and seven female subjects with a mean age of 53 years (range 16–76 years). MRI findings, evaluated by two radiologists with agreement by consensus, were compared for histopathologic features. *Results:* The tumor size ranged from 2.0 cm to 20.0 cm (mean 8.9 cm). Fusion gene transcripts could be detected in 13 (68%) of the 19 cases: EWS-CHN in nine cases, TAF2N-CHN in three, and TFG-TCH in one. There were six fusion-negative cases. Signal characteristics on T1-weighted and T2-weighted MR images were non-specific with regard to each cytogenetic variant. Peripheral enhancement was seen more frequently in tumors with the EWS-CHN variant than in those with other cytogenetic variants. The characteristic pattern of enhancement corresponded to the presence of fibrous septa and peripheral areas of high cellularity within lobules, by correlation with pathologic findings. All cases with TAF2N-CHN or TFG-TCH variants showed invasion of extracompartmental structure, bone, or vessels. *Conclusion:* Extraskeletal myxoid chondrosarcoma is an uncommon soft-tissue malignancy that may be recognized by MRI features of multilobular soft-tissue mass often invading extracompartmental, bony, and vascular structures.

Keywords Extraskeletal myxoid chondrosarcoma · MRI · Cytogenetic variant

Introduction

Extraskeletal myxoid chondrosarcoma (EMC) is a rare malignant soft-tissue tumor characterized by abundant myxoid matrix and malignant chondroblastic cells [1, 2]. EMC mostly arises in the deep soft tissue of the proximal extremities and limb girdles and comprises multiple gelatinous nodules divided by fibrous septa. Although the most common manifestation is an enlarging soft-tissue mass, some lesions are accompanied by pain and tenderness or may restrict the range of motion. Long-term follow-up studies have shown that EMC is a slowly growing tumor with a risk of local recurrence or distant metastasis. EMC is a tumor with long survival but is known to have a potential for local recurrence, metastasis, and a disease-associated death [1–4].

EMC was described as a distinct entity, precisely, by Enzinger and Shiraki [5]. Subsequent clinicopathologic and molecular studies have yielded findings consistent with the distinct tumor characteristics and have revealed that EMC is composed of at least four cytogenetic variants: EWS-CHN, TAF2N-CHN, TCF12-CHN, TFG-TCH [6-11]. These variants were derived from independent chromosomal translocations and the resultant fusion genes. The identification of the highly specific balanced chromosomal rearrangement in EMC assists a specific diagnosis at molecular level.

The typical radiographic manifestation of EMC is that of a large, well-demarcated mass, partially contained by pseudocapsule, with associated intratumoral cysts and hemorrhage. A few reports on case series of EMC had been published at the time this article was written [12–14]. In addition, the relationship between cytogenetic variants and imaging findings were not fully understood.

The purpose of our study was to describe the imaging features of EMC in comparison with clinicopathologic findings.

Materials and methods

Nineteen cases of EMC were retrieved from the pathology files of our institute. Patients were identified from a pathologic registration system database through a query for patients with diagnosed EMC who had undergone surgical resection. A reference pathologist reviewed all cases to confirm the histologic diagnosis based on current standards. Clinical information was extracted from the patient files regarding patient age, gender, symptoms, treatment, local recurrences, metastases, metastatic sites, associated conditions, and final disease status. Our institutional review board does not require its approval or patients' informed consent for this type of review.

Radiologic studies of each lesion were reviewed by two radiologists, with consensus, and included CT, with (n=4) and without (n=15) contrast material enhancement, and MRI with high-field (1.5-T) units in all patients. T1-weighted and T2-weighted images were obtained in the transverse plane and in at least one longitudinal plane with either a surface coil (n=15) or a body coil (n=4). T1-weighted fast spin-echo images were obtained by using a 24–30 cm field of view, 4–8 mm section thickness, 400–620 ms/8.9–15 ms repetition time/echo time, 256×192–224 matrix, two signals acquired. T2-weighted fast spin-echo acquisitions were performed by using a 24–35 cm field of view, 4–8 mm section thickness, 3,000–6,220 ms/84–120 ms repetition time/echo time, 256×192–224 matrix, two signals acquired. After the intravenous administration of 0.1 mmol of gadopentate dimeglumine (Magnevist, Schering, Berlin, Germany) per kilogram of body weight, transverse T1-weighted images with fat suppression were obtained in the transverse plane and in at least one longitudinal plane.

Images were evaluated for lesion location and size, depth (superficial or deep), shape of margin (well-defined or ill-defined), and the presence or absence of extracompartmental extension. Mineralized matrix was assessed on CT images. MR images were evaluated for predominant signal intensity characteristics (low, intermediate, or high), signal homogeneity or heterogeneity, as well as enhancement characteristics. On T1-weighted images low signal intensity was defined as signal intensity less than that of muscle; intermediate signal intensity, similar to that of muscle; and high signal intensity, similar to that of fat. On T2-weighted images, low signal intensity was defined as signal intensity similar to that of muscle; intermediate signal intensity, greater than that of muscle but less than that of fat; and high signal intensity, equal to or greater than that of fat. Tumor enhancement was visually graded as greater than, less than, or equal to, that of surrounding muscle and vessels. The pattern and homogeneity of enhancement were also recorded: peripheral, diffuse, and mixed patterns. Peripheral enhancement was assigned when the curvilinear enhancing septal areas were present within tumor. Cortical destruction and vascular encasement were also evaluated.

For reverse-transcribed polymerase chain reaction (RT-PCR) analysis, frozen tissues were available from 18 patients. The RNA was reverse transcribed, and the samples were then subjected to protein chain reaction (PCR) amplification using primers: CCCACTAGTTACCCAC CCCA (EWS exon 7 forward); TCTGGCAGACTTCTTT TAAGCA (EWS exon 11 forward); GCGATGCCACAGT GTCCTATG (EWS exon 12 forward); GAGCAGTCAA ATTATGATCAGCAGC (TAF2N forward); GCAACA ACGCATGGCCGCTAT (TCF12 forward); AGCTTGG AACCACCTGGAGAACC (TFG forward); GCTGTAT GTCTGCGCCGCATAACT (CHN-1 reverse); TCTCAG CCTCCGCTGGAGAGA (CHN-2 reverse). Specimens were fixed with formalin and sectioned in the same plane as that of the CT and MR images. The specimens were stained with hematoxylin–eosin, and immunohistochemical staining was also performed. In one patient whose frozen tissue was not available, fluorescence in situ hybridization (FISH) was performed to detect EWS gene aberrations in formalin-fixed paraffin-embedded tissue. Tumor specimens were immunostained with the antibody Ki-67 (Dako; diluted 1:100 and autoclaved), and the Ki-67 (MIB-1) labeling index (LI) was estimated by determining the percentage of Ki-67-positive cell nuclei per 1,000 tumor cells in the region of the tumor with the greatest density of ki-67 staining viewed under a light microscope. Both MIB-1 grade (MIB-1 grading system) and mitosis grade (the modified French system) are three-grade systems obtained by summing the scores of tumor differentiation, tumor necrosis, and the MIB-1 score or mitotic score, each of which was given a score of 0, 1, 2, or 3. Tumor differentiation score, according to histologic type, was modified slightly from the French system. The mitotic figures were counted on routine hematoxylin and eosin

Table 1 Cytogenetic variants of EMC (*T1WI* T1-weighted image, *T2WI* T2-weighted image, *NOS* not otherwise specified

Variant	Translocation	Number	T1WI	T2WI	Gadolinium enhancement	Extracompartmental extension	Bone invasion	Vascular invasion
EWS-CHN	t(9;22) (q22;q12)	9	Intermediate: 6 High: 3	Intermediate: 1 High: 8	Peripheral: 5 Mixed: 4	2	3	1
TAF2N-CHN	t(9;17) (q22;q11)	3	Intermediate: 2 High: 1	High: 3	Diffuse: 2 Mixed: 1	2	0	1
TFG-TCH	t(3;9) (q11;q22)	1	High: 1	Intermediate: 1	Mixed: 1	0	1	0
NOS	–	6	Intermediate: 6	Intermediate: 2 High: 4	Mixed: 3 Diffuse: 2 Peripheral: 1	1	1	2

stained sections. The areas selected for cell counting were from the most mitotically active parts of the tumors, usually located at the periphery. The mitotic score was assessed by counting the number of mitotic figures in ten consecutive high-power fields. The MIB-1 score was estimated by counting the percentage of MIB-1-positive cell nuclei per 1,000 tumor cells in the region of the tumor with the greatest density of staining, which, in most instances, corresponded to the areas with the highest mitotic activity. In this study the histological grade of a tumor was determined by a three-grade system in which tumor differentiation, tumor necrosis, and MIB-1 LI, were each given a score of 0, 1, 2, or 3 and then added together. Lesions with MIB-1 LIs of 0–9%, 10–29%, or greater than 30% were assigned MIB-1 scores of 1,2 or 3, respectively. The three separate scores were added together to produce a combined grade: lesions with a total score of 2 or 3 were classified as grade 1, those that scored 4 or 5 were grade 2, and those that scored 6,7 or 8 were grade 3. According to this MIB-1 system, tumors were assigned grades 1–3. The cut surface, internal characteristics, and microscopic findings of the lesions were compared with those seen on CT and MR images. Correlation between the imaging and histologic findings was made by consensus between the radiologist and pathologist.

Follow-up information was available in all cases. Deaths confirmed to be caused by disease were treated as an end point, whereas deaths from other causes were treated as censored observations. The disease-free date was considered to be the date when the medical record documented no

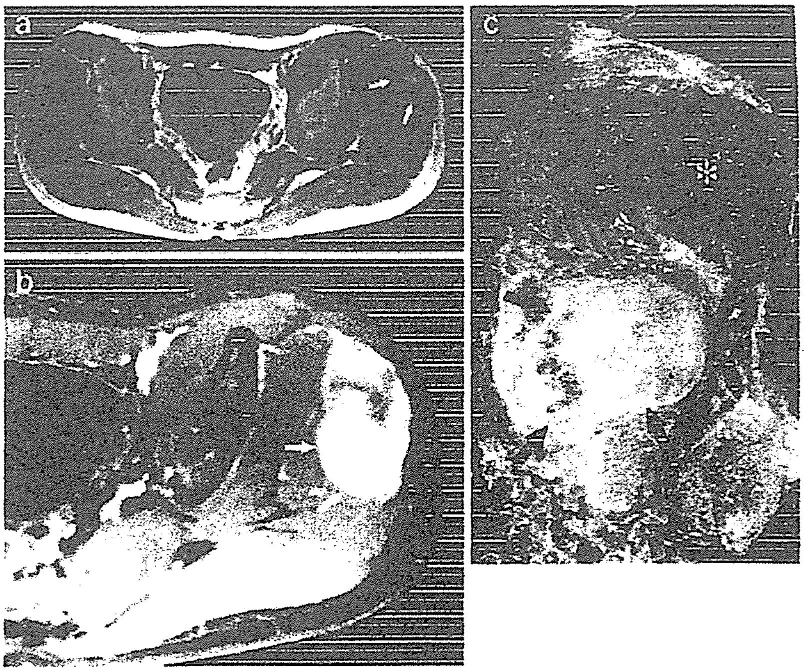

Fig. 1 A 46-year-old man with the TAF2N-CHN variant of EMC arising from the left gluteal region. **a** Transverse, T1-weighted (500 ms/15 ms), MR image shows a focus of high signal intensity within the tumor (*arrows*), resulting from hemorrhage. **b** Transverse, fat-saturated, T1-weighted (600 ms/12 ms), MR image after contrast enhancement demonstrates moderate enhancement of the tumor. The enhancement of hemorrhagic areas (*asterisk*) was depicted more heterogeneously than those of solid portions (*arrows*). **C** Sectioned gross specimen reveals hemorrhagic areas (*asterisk*) and solid portions (*arrows*) admixed with extensive myxoid stroma corresponding to the MRI appearance

evidence of disease. Recurrence was assigned when the patient developed recurrent tumor related to surgical margins. Metastasis was assigned when the patient developed distant a metastasis, including bone and lung metastases, during the course of the disease and did not contain the case with recurrence.

Results

There were 12 male (63%) and seven female (37%) patients aged from 16 years to 76 years, with an average age of 53 years. The arising sites of soft-tissues were calf (*n*=5), foot (*n*=4), buttock (*n*=3), thigh (*n*=3), groin (*n*=1), shoulder (*n*=1), arm (*n*=1), and hand (*n*=1). Presenting symptoms were stated in all patients. The most common symptom was a mass that had enlarged (*n*=15). Four patients had evidence of pain or tenderness. There were three cytogenetic variants in 13 cases (68%): EWS-CHN in nine cases, TAF2N-CHN in three, and TFG-TCH in one, and not otherwise specified in six cases (Table 1). There were 11 grade 1 tumors and eight grade 2 tumors as assigned by the MIB-1 grading system.

The mean diameter of tumors was 8.9 cm (range 2.0–20.0 cm). The location of the tumor was superficial in four patients (27%), while the remaining 11 (73%) were distributed deeply. Mineralized matrix that was centrally located within the tumor was seen in one case on non-enhanced CT images. Multi-nodular soft-tissue masses with well-defined (*n*=5, 26%) or ill-defined (*n*=14, 74%) margins were seen on CT and MR images. One patient (5%) demonstrated a metastatic lesion at initial presentation.

MR images showed predominantly intermediate (*n*=14, 74%) and high (*n*=5, 26%) signal intensity relative to muscle on T1-weighted MR images, with one lesion also demonstrating areas of focal high signal intensity, reflecting the hemorrhagic region (Fig. 1). On T2-weighted MR images, signal intensity was heterogeneous in all patients. Fifteen lesions (79%) had high signal intensity, equal to or greater than that of fat. The remaining four lesions (21%) had intermediate signal intensity, greater than that of muscle but less than that of fat. Signal characteristics on T1-weighted and T2-weighted MR images were nonspecific with regard to each cytogenetic variant.

All lesions demonstrated mild-to-moderate and heterogeneous enhancement of the tumor after intravenous administration of a gadolinium-based contrast agent. Solid components of the tumors showed peripheral enhancement (*n*=6, 32%, Fig. 2), diffuse enhancement (*n*=4, 21%, Fig. 3), and a mixed pattern of enhancement (*n*=9, 47%). Peripheral enhancement was seen more frequently in tumors with the EWS-CHN variant than in those with other cytogenetic variants ($P<0.05$).

Ulceration of the tumor surface was identified in one case. Vascular encasement was seen in four cases, and one of those cases was accompanied by intravenous tumor extension. Tumors showed extracompartmental extension in five patients. Cortical destruction with soft-tissue mass was seen in five patients. Of these, a tumor arising from the back showed intraforaminal extension to the spinal canal, with marked bone destruction. All cases with TAF2N-CHN

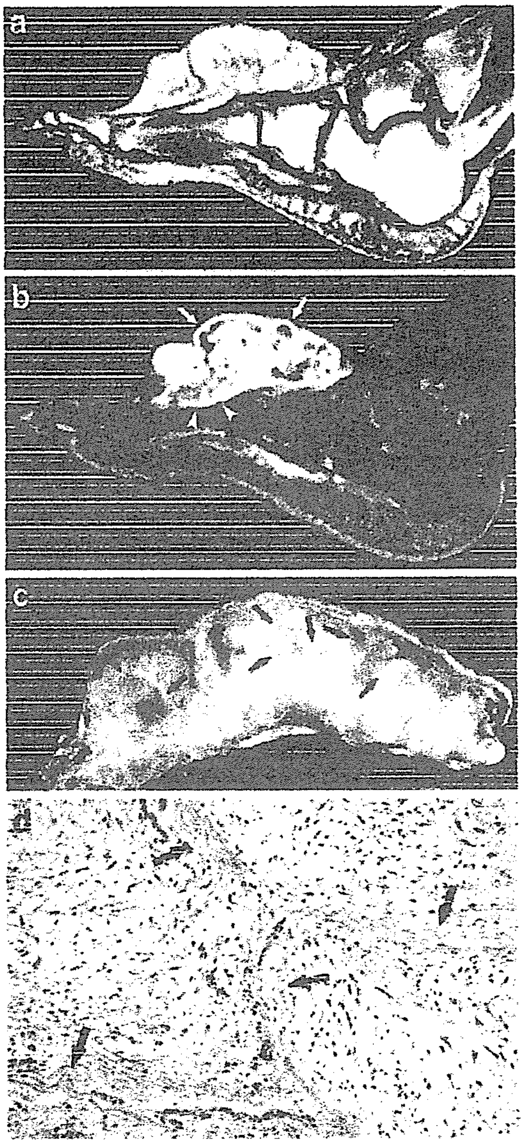

Fig. 2 A 76-year-old woman with the EWS-CHN variant of EMC of the foot. **a** Sagittal, T2-weighted (3,000 ms/102 ms), MR image shows a well-defined mass, involving the foot, with high signal intensity greater than that of subcutaneous fat. **b** Sagittal, fat-saturated, T1-weighted (600 ms/15 ms), MR image after contrast administration shows peripheral enhancement (*arrows*). Also noted is extracompartmental growth beyond fascia (*arrowheads*). **c** Sagittally sectioned gross specimen shows myxoid and gelatinous nodules separated by fibrous septa (*arrows*). **d** Photomicrograph of the specimen demonstrates mature hyaline cartilage with fibrous tissue and myxoid stroma corresponding to the MRI appearance (H & E, original magnification ×100)

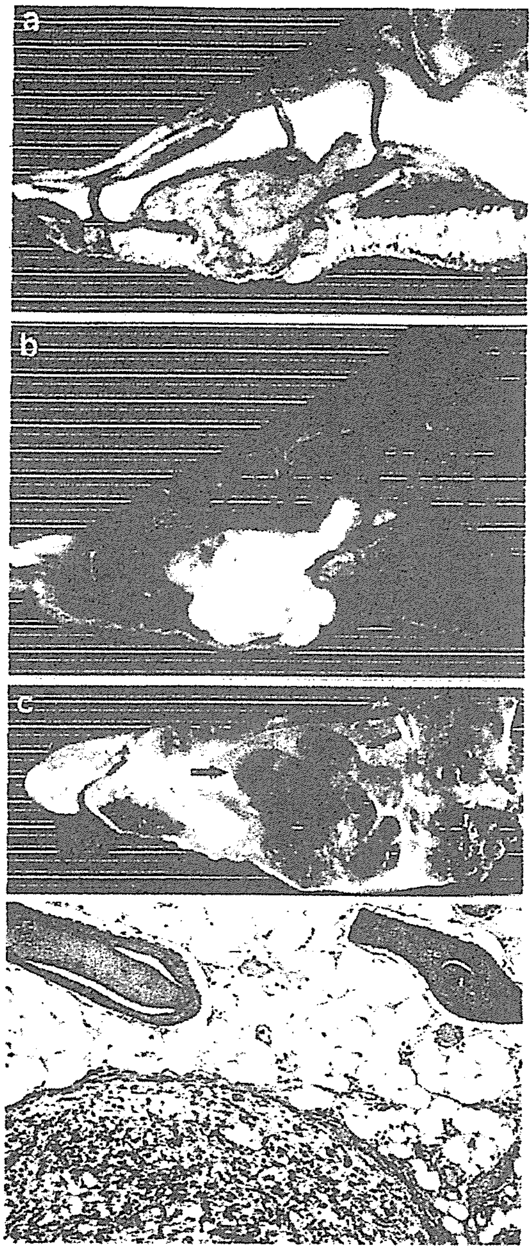

Fig. 3 A 61-year-old woman with the TFG-TCH variant of EMC manifesting as extracompartmental extension. **a** Sagittal, T2-weighted (4,000 ms/89.9 ms), MR image shows a poorly defined mass involving the sole, with intermediate signal intensity less than that of subcutaneous fat. **b** Sagittal, fat-saturated, T1-weighted (600 ms/15 ms), MR image after administration of contrast material shows diffuse enhancement. **c** Sagittal plane of pathology specimen reveals extracompartmental growth (*arrows*) and destruction of calcaneous bone (*asterisk*). **d** Photomicrograph of the specimen shows nodular architecture of marrow invasion (H & E, original magnification ×100)

or TFG-TCH variants showed invasion of extracompartmental structure, bone, or vessels.

Gross characteristics of resected specimens featured multi-nodular architecture corresponding to the cross-sectional MRI features. In all cases the cut surface of specimens revealed myxoid and gelatinous nodules separated by fibrous septa, which corresponded to the appearance of various signal characteristics on T1-weighted and T2-weighted MR images. Fibrous septa also corresponded to areas of peripheral enhancement on contrast-enhanced MR images. Heterogeneous enhancement on contrast enhanced MR images also correlated with the presence of intratumoral cysts (n=4) and hemorrhage (n=1). These areas corresponded to areas of high signal intensity on T2-weighted MR images. Geographic areas of necrosis were present in five patients (26%). Lobules often showed higher cellularity at the periphery, which corresponded to peripheral or diffuse enhancement on contrast-enhanced MR images. Hyaline cartilage had developed in one patient, although there were small islands of immature cartilage in several patients. All tumors were characterized microscopically by cords or clusters of neoplastic cells, which demonstrated a modest amount of eosinophilic, granular-to-vacuolated cytoplasm and uniform ovoid nuclei. Fourteen tumors were assigned grade 1 malignancy, and the remaining six tumors were grade 2.

All patients underwent surgical resection as a primary therapy. Surgical margins were adequate in 11 patients and inadequate in four. All patients with inadequate surgical margins had undergone subsequent wide resection. Chemotherapy (carboplatinum 1,000 mg, Adriamycin 60 mg) and radiotherapy (50 Gy) were included in the treatment regimen of one patient. The median follow-up period of all cases was 61 months. There were local recurrences in three patients (16%) at a median interval of 12 months. Metastases occurred in three cases (16%). The sites of metastases were lungs (n=3) followed by bone (n=1). Two patients that were being followed-up had died from the disease; 17 patients were alive with the disease or with no evidence of disease.

Discussion

EMC has been described as a rare, adult, soft-tissue sarcoma. It commonly affects patients aged 50–60 years but is also known to occur in younger people [1, 2]. Patients usually present with non-specific symptoms, including tenderness and palpable mass [1–4]. Patient demographics and clinical symptoms in our series were similar to those in previous studies [1, 2].

Unlike in the previous reports [12–14], signal characteristics on T1-weighted MR images were varied. In our study, tumors showed predominantly low (5%), intermediate (80%), or high (15%) signal intensity relative to muscle on T1-weighted MR images. These features on T1-

weighted MR images might be due to underlying pathologic changes. In all our cases, myxoid and gelatinous nodules, separated by fibrous septa, were frequently apparent on pathologic observation. Pathologically, EMC often consists of hemorrhagic changes [2]. MRI evidence of hemorrhagic foci of high signal intensity on T1-weighted image was seen in one of our patients. Although this was in accordance with pathologic findings, the occurrence of hemorrhage was not a common finding on MR images.

A few case series have demonstrated homogeneous or heterogeneous enhancement on contrast-enhanced MR images [12–14]. In fact, all our cases showed heterogeneous enhancement. Peripheral enhancement was also found in 32% of our cases after administration of contrast material at MRI. These results suggest that the enhancement pattern on MR images may depend on tumor heterogeneity in EMC. The high frequency of peripheral enhancement that was demonstrated on contrast-enhanced T1-weighted MR images was in good accordance with the gross pathologic features.

High signal intensity on T1- weighted images corresponded to areas of hemorrhage identified pathologically, as described in our study. Although intratumoral hemorrhage was found in only one case, hemorrhagic soft-tissue sarcoma could be considered in the differential diagnosis. Synovial sarcoma is often associated with hemorrhagic change, representing various MR signal patterns. Triple-signal pattern, one of the heterogeneous patterns on T2-weighted MR images, is considered to be not specific but suggestive of the diagnosis, given the most prevalent age [15]. Fluid–fluid levels may occur whenever substances of differing densities are contained within a cystic or compartmentalized structure. The levels are depicted when imaging is performed in a gravity-dependent plane. The presence of fluid–fluid levels in soft-tissue tumors cannot be considered diagnostic of any particular tumor, including synovial sarcoma and malignant fibrous histiocytoma [16]. A sign of fluid–fluid level was seen in none of our cases on T2-weighted MR images, which would suggest that this finding might be less frequent in patients with EMC.

The identification of the highly specific balanced chromosomal rearrangement in EMC provides a valuable tool for diagnosis at the molecular level. In our series, 68% of tumors consisted of three variant fusions. The relationship between cytogenetic variants and imaging findings were not fully understood. Although signal characteristics on T1-weighted and T2-weighted MR images were non-specific, peripheral enhancement on contrast-enhanced MR images was seen more frequently in tumors with the EWS-CHN variant than in those with other cytogenetic variants, according to our results. Peripheral enhancement on contrast-enhanced MR images may be characteristic for this entity, because most patients with EMC have chromosomal aberration of EWS-CHN [6–11].

The imaging features of EMC reflect the underlying pathologic findings [12–14]. Extracompartmental extension and cortical destruction, with soft-tissue mass, were found in 26% of cases, according to our results. In addition, all tumors with TAF2N-CHN or TFG-TCH variants showed invasion of extracompartmental structure, bone, or vessels. Although the association between imaging findings and cytogenetic variants is obscure, the invasive nature of MRI findings may be characteristic in these variants.

As with other soft -tissue sarcomas in adults, surgical resection is recommended in EMC. EMC typically has a prolonged clinical course with complete resection [4]. However, the behavior of EMC has been reported to be poor, with frequent local recurrences and distant metastases [1, 3]. Sixteen percent of our patients developed local recurrences, and metastases occurred in 16% of our cases. EMC seems to have frequent recurrences and metastases, and long-term follow-up is needed.

We recognize certain limitations of our study. Because of the referral basis of our cases, we were unable to control the MRI parameters. However, our retrospective review includes a greater number of cross-sectional imaging studies than does any previous study [5–8]. Despite these limitations, our study may add substantial understanding of imaging features of EMC.

Conclusion

Characteristic imaging features of EMC are multi-nodular soft-tissue masses, presenting predominantly hyper-signal intensity on T2-weighted MR images and heterogeneous enhancement after administration of contrast material. Peripheral enhancement was seen more frequently in tumors with the EWS-CHN variant than in those with other cytogenetic variants. Tumors with TAF2N-CHN or TFG-TCH variants showed invasion of extracompartmental structure, bone, or vessels. These features clearly reflect the underlying histopathologic characteristics of EMC.

References

1. Saleh G, Evans HL, Ro JY, Ayala AG. Extraskeletal myxoid chondrosarcoma. A clinicopathologic study of ten patients with long-term follow-up. Cancer 1992;15 70:2827–30
2. Meis-Kindblom JM, Bergh P, Gunterberg B, Kindblom LG. Extraskeletal myxoid chondrosarcoma: a reappraisal of its morphologic spectrum and prognostic factors based on 117 cases. Am J Surg Pathol 1999;23:636–50
3. Lucas DR, Fletcher CD, Adsay NV, Zalupski MM. High-grade extraskeletal myxoid chondrosarcoma: a high-grade epithelioid malignancy. Histopathology 1999;35:201–8

4. Kawaguchi S, Wada T, Nagoya S, et al. Extraskeletal myxoid chondrosarcoma: a multi institutional study of 42 cases in Japan. Cancer 2003;1 97:1285–92
5. Enzinger FM, Shiraki M. Extraskeletal myxoid chondrosarcoma. An analysis of 34 cases. Human Pathol 1972;3: 421–35
6. Okamoto S, Hisaoka M, Ishida T, et al. Extraskeletal myxoid chondrosarcoma: a clinicopathologic, immunohistochemical, and molecular analysis of 18 cases. Human Pathol 2001;32:1116–24
7. Sjögren H, Meis-Kindblom JM, Orndal C, et al. Studies on the molecular pathogenesis of extraskeletal myxoid chondrosarcoma—cytogenetic, molecular genetic, and cDNA microarray analyses. Am J Pathol 2003;162: 781–92
8. Sjögren H, Mei-Kindblom J, Kindblom LG, Aman P, Stenman G. Fusion of EWS-related gene TAF2N to TEC in extraskeletal myxoid chondrosarcoma. Cancer Res 1999;59:5064–7
9. Bjerkehagan B, Dietrich C, Reed W, et al. Extraskeletal myxoid chondrosarcoma: multimodal diagnosis and identification of a new cytogenetic subgroup characterized by t(9;17)(q22;q11). Virchows Arch 1999;435:524–30
10. Panagopoulos I, Mertens F, Isaksson M, et al. Molecular genetic characterization of the *EWS/CHN* and *RBP6/CHN* fusion genes in extraskeletal myxoid chondrosarcoma. Genes Chromosomes Cancer 2002;35:340–52
11. Hisaoka M, Ishida T, Imamura T, Hashimoto H. TFG is a novel fusion partner of NOR1 in extraskeletal chondrosarcoma. Genes Chromosomes Cancer 2004;40:325–8
12. Gebhardt MC, Parekh SG, Rosenberg AE, Rosenthal DI. Extraskeletal myxoid chondrosarcoma of the knee. Skeletal Radiol 1999;28:354–8
13. Okamoto S, Hara K, Sumita S, et al. Extraskeletal myxoid chondrosarcoma arising in the finger. Skeletal Radiol 2002;31:296–300
14. Murphey MD, Walker EA, Wilson AJ, Kransdorf MJ, Temple HT, Gannon FH. From the archives of the AFIP: imaging of primary chondrosarcoma: radiologic–pathologic correlation. Radiographics 2003;23:1245–78
15. Jones BC, Sundaram M, Kran3dorf MJ. Synovial sarcoma: MR imaging findings in 34 patients. AJR Am J Roentgenol 1993;161:827–30
16. Morton MJ, Berquist TH, McLeod RA, et al. MR imaging of synovial sarcoma. AJR Am J Roentgenol 1991; 156:337–40

Available online at www.sciencedirect.com

SCIENCE DIRECT®

European Journal of Pharmacology 510 (2005) 217–222

www.elsevier.com/locate/ejphar

Short communication

Capacitative Ca^{2+} entries and mRNA expression for TRPC1 and TRPC5 channels in human epidermoid carcinoma A431 cells

Junko Yoshida[a,*], Takaharu Ishibashi[a], Noriko Imaizumi[b], Tsutomu Takegami[c], Matomo Nishio[a]

[a] *Department of Pharmacology, Kanazawa Medical University, Uchinada, Ishikawa 920-0293, Japan*
[b] *Division of Endocrinology, Department of Internal Medicine, Kanazawa Medical University, Uchinada, Ishikawa 920-0293, Japan*
[c] *Division of Molecular Oncology and Virology, Medical Research Institute, Kanazawa Medical University, Uchinada, Ishikawa 920-0293, Japan*

Received 14 January 2005; accepted 20 January 2005

Abstract

In human epidermoid carcinoma A431 cells, capacitative Ca^{2+} entries in response to intracellular Ca^{2+} store depletion with thapsigargin, an endoplasmic reticulum Ca^{2+}-ATPase inhibitor, and uridine 5′-triphosphate, a phospholipase C-linked agonist, were inhibited by trivalent cations such as Gd^{3+} and La^{3+}, and by the store-operated Ca^{2+} channel inhibitor, 2-aminoethoxydiphenyl borate. Of the seven types of canonical transient receptor potential (TRPC) channels as molecular candidates for store-operated Ca^{2+} channels, mRNAs for TRPC1 and TRPC5 were detected in the cells with the reverse transcription-polymerase chain reaction. Western blotting confirmed the protein expressions of TRPC1 and TRPC5 in A431 cells. The present results suggest that TRPC1 and/or TRPC5 channels serve as store-operated Ca^{2+} channels in A431 cells, and may function as regulators for intracellular Ca^{2+} signaling.

Keywords: TRPC1; TRPC5; Capacitative Ca^{2+} entry; Human epidermoid carcinoma A431 cell; Thapsigargin; Uridine 5′-triphosphate

1. Introduction

Intracellular Ca^{2+} is indispensable for the proliferation of various cell types. The cytosolic free Ca^{2+} concentration ($[Ca^{2+}]_i$) is controlled by Ca^{2+} entry pathways in the plasma membrane and Ca^{2+} release from internal Ca^{2+} stores localized in the sarco(endo)plasmic reticulum. There are at least two classes of Ca^{2+}-permeable channels in the plasma membrane: voltage-dependent Ca^{2+} channels (VDCCs) and non-voltage-gated Ca^{2+}-permeable channels, such as store-operated Ca^{2+} channels (SOCs) or receptor-activated cation channels. The latter class of channels are activated by the depletion of intracellular Ca^{2+} stores and evoke capacitative Ca^{2+} entry (Putney et al., 2001).

In previous studies, we found that dihydropyridine Ca^{2+} channel blockers such as amlodipine inhibited the growth of human epidermoid carcinoma A431 cells in vitro (Yoshida et al., 2003; Yoshida et al., 2004), though this cell line lacks dihydropyridine-sensitive VDCCs (Moolenaar et al., 1986). Fluorometric measurements of $[Ca^{2+}]_i$ revealed that amlodipine specifically attenuated the capacitative Ca^{2+} entries elicited by thapsigargin, an endoplasmic reticulum Ca^{2+}-ATPase (Yoshida et al., 2003), and UTP, a phospholipase C (PLC)-linked agonist. Thus, we suggested that the anti-proliferative actions of some dihydropyridine Ca^{2+} channel blockers, such as amlodipine, may be partly mediated by inhibiting capacitative Ca^{2+} entry through SOCs in the plasma membrane of A431 cells (Yoshida et al., 2004).

Although the molecular identity of I_{SOC} channels in A431 cells has not yet been determined, mammalian homologs of the *Drosophila* canonical transient receptor potential (TRPC) channel family have been implicated as molecular candidates for SOCs and receptor-activated cation channels in both excitable and non-excitable tissues (Ma et al., 2000; Vennekens et al., 2002). It is plausible that TRPC channels are expressed in A431 cells and may function as

---

* Corresponding author. Tel.: +81 76 286 2211x3724; fax: +81 76 286 8191.

E-mail address: yayuyo@kanazawa-med.ac.jp (J. Yoshida).

0014-2999/$ - see front matter © 2005 Elsevier B.V. All rights reserved.
doi:10.1016/j.ejphar.2005.01.029

SOCs. To explore the possible mechanisms underlying the antiproliferative action of amlodipine, we examined the properties of thapsigargin- and UTP-induced capacitative Ca^{2+} entries by means of single-cell Ca^{2+} imaging and mRNA expression for the seven types of human TRPC (hTRPC1–7) in A431 cells by the reverse transcriptional polymerase chain reaction (RT-PCR).

2. Materials and methods

2.1. Reagents

Thapsigargin was dissolved in dimethyl sulfoxide (DMSO) at a concentration of 10 mM. UTP and SKF 96365 (Sigma-Aldrich Co.) were dissolved in distilled water at concentrations of 100 mM and 10 mM, respectively. 2-Aminoethoxydiphenyl borate (2-APB; Tocris Cookson Inc., Ellisville, MO, USA) was dissolved in DMSO (100 mM). Anti-TRPC1 and anti-TRPC5 antibodies were purchased from Alomone Labs Ltd. (Jerusalem, Israel).

2.2. Tumor cell lines

Human epidermoid carcinoma A431 cells, kindly supplied by Professor Katsuzo Nishikawa (The Second Department of Biochemistry, Kanazawa Medical University), were cultured as described previously (Yoshida et al., 2001; Yoshida et al., 2003, 2004). Briefly, the cells were cultured in Dulbecco's modified Eagle medium (DMEM), containing 10% heat-inactivated fetal bovine serum, 2 mM L-glutamine, 12.7 mM 4-(2-hydroxyethyl)-1-piperazineethanesulfonic acid (HEPES), 0.12% sodium bicarbonate, 100 U/ml penicillin G and 100 μg/ml streptomycin, at 37 °C in humidified air containing 5% CO_2. Cells were seeded at a density of 3×10^5/plate in 10 cm diameter plastic culture dishes and passaged every 3–4 days.

2.3. Measurement of intracellular free Ca^{2+} concentrations

The microscopic fluorometric measurement of intracellular free Ca^{2+} concentrations ($[Ca^{2+}]_i$) was performed as described previously (Yoshida et al., 2004). Briefly, A431 cells, grown on poly-D-lysine coated glass bottom dishes (MatTek, Ashland, MA, USA), were washed with a HEPES-buffered physiological saline solution (HBSS) (in mM: 130 NaCl, 2.5 KCl, 1.2 $MgCl_2$, 10 HEPES, 10 glucose, and 2 $CaCl_2$, pH adjusted to 7.4 with NaOH) and loaded with 3 μM acetoxymethyl ester of fluo-3 (fluo-3/AM: Dojindo Laboratories, Kumamoto, Japan) containing 0.005% Cremophore EL (Sigma-Aldrich Co.) for 30 min in the dark at room temperature (25 ± 2 °C). Cells were post-incubated in HBSS for 30 min. In the experiment, the cells were washed with Ca^{2+}-free HBSS, and then the dishes were placed on a Nikon inverted microscope (ECLIPSE TE 300, Nikon, Tokyo, Japan) equipped with a Nikon ×40 S-fluor objective. Fluorescence images of the cells were recorded and analyzed with a video image analysis system (ARGUS/HiSCA, Hamamatsu Photonics, Hamamatsu, Japan). The agents in volumes of 20–100 μl were sequentially applied to the cells bathing in 2 ml of recording medium. Image pairs were captured at 10-s intervals. Fluo-3 fluorescence was monitored at an emission wavelength of 527 nm by exciting fluo-3 at 480 nm. Normalized fluorescent intensities of $F480/F480_0$ were used to indicate changes in $[Ca^{2+}]_i$, where $F480_0$ indicates basal fluorescence.

2.4. RNA preparation and RT-PCR

Total RNA was extracted from A431 cells using the ISOGEN reagent (Nippon Gene, Tokyo, Japan). First-strand cDNA was synthesized from the RNA preparations with a ProSTAR™ First-Strand RT-PCR Kit (Stratagene, La Jolla, CA, USA); RNA (10 μg) was reverse transcribed using the oligo(dT) primer (6 ng/μl) in a total volume of 50 μl. To perform PCR amplifications, the following sets of primers were used: TRPC1 (accession no. U31110): forward 5′CAA GAT TTT GGA AAA TTT CTT G 3′, reverse 5′ TTT GTC TTC ATG ATT TGC TAT 3′ (PCR product, 372 bp); TRPC3 (accession no. Y13758): forward 5′ TGA CTT CCG TTG TGC TCA AAT ATG 3′, reverse 5′ TCT GAA GCC TTC TCC TTC TGC 3′ (PCR product, 315 bp); TRPC4 (accession no. X90697): forward 5′ TCT GCA GAT ATC TCT GGG AAG GAT GC 3′, reverse 5′ AAG CTT TGT TCG AGC AAA TTT CCA TTC 3′(PCR product, 415 bp); TRPC5 (accession no. AF054568): forward 5′ GTT CCT GTT TCC CAT GCT GT 3′, reverse 5′ AGT GCT TCC GCA ATC AGA GT 3′ (PCR product, 429 bp); TRPC6 (accession no. U49069): forward 5′ GCT CAT CCA AAC TGT CAG CA 3′, reverse 5′ CAG CAT TCC AAA GTC AAG CA 3′ (PCR product, 468 bp); TRPC7 (accession no. AJ272034): forward 5′ GCT GCC TAC TTG TCC CTG TC 3′, reverse 5′ AAA AGG GAG GCC TAT GGA GA 3′ (PCR product, 411 bp); VDCC (accession no. L04569): forward 5′ AGT CCG TCA ACA CCG AAA AC 3′, reverse 5′ CCA GTT GGG CTG GTT GTA GT 3′ (PCR product, 239 bp); VDCC (accession no. U95019): forward 5′ GTA CCT TCC ATG CGA CCA GT 3′, reverse 5′ TCC GCT AAG CTT GAC CTT GT 3′ (PCR product, 227 bp); hGAPDH (accession no. AB062273): forward 5′ CCA CCC ATG GCA AAT TCC ATG GCA 3′, reverse 5′ TCT AGA CGG CAG GTC AGG TCC ACC 3′ (PCR product, 598 bp). All primers were obtained from the Hokkaido System Science Co. Ltd. (Sapporo, Japan). PCR was performed on 1–2 μl cDNA from A431 cells with a HotStarTaq Master Mix Kit (QIAGEN K.K., Tokyo, Japan) in a total volume of 25 μl. Human brain first strand cDNA (Adult male, Stratagene) and cDNA from NCI-H295 human adrenocortical carcinoma cells, prepared using the same procedure for A431 cells, were used as positive control samples. A negative control was included in each PCR reaction whereby cDNA was replaced with ultrapure water. Each reaction was performed in the presence of 1 μM 5′ and 3′ gene-specific primers. The PCR program consisted of an initial denaturation at 95 °C for 15 min, 35 cycles at 94 °C for 1 min, 60 °C (50 °C for hTRPC1) for 1 min, and 72 °C for 1 min, and a final extension step at 72 °C for 10 min. PCR products were separated by 1.5–2.0% agarose gel electrophoresis and visualized by ethidium bromide staining.

2.5. Western blot analysis

Cultured A431 cells were lysed in 0.5 ml of mammalian cell lysis/extraction reagent (CelLytic™-M; Sigma-Aldrich Co.) containing protease inhibitors (Protease inhibitor cocktail; Sigma-Aldrich Co.), 1 mM phenylmethylsulfonyl fluoride and 1 mM Na_3VO_4 by repeated passage through a 23-gauge needle. The lysate was centrifuged at 12,500×*g* for 15 min at 4 °C to remove insoluble material, and the protein concentration of the supernatant was determined with the Bio-Rad protein assay reagent (Bio-Rad Laboratories, CA, USA). The cell lysate (25 μg protein) was denatured in 5× sample buffer (625 mM Tris–HCl, 10% SDS, 25% glycerol, 0.015% bromophenol blue and 5% 2-mercaptoethanol, pH 6.8) at 95 °C for 5 min, then electrophoretically separated on a 4–20% polyacrylamide gel (PAG Mini "DAIICH" 4/20: DAIICHI Pure Chemical Co., Ltd., Tokyo, Japan), and the protein bands were transferred to a nitrocellulose membrane. The membrane was blocked with phosphate buffered saline (PBS) containing 5% non-fat milk and 0.1% Tween 20, and subsequently probed with polyclonal antibodies to TRPC1 and TRPC5 (1:200; Alomone Labs, Jersalem, Israel) for 40 min at room temperature. Following a wash with PBS containing 0.1% Tween 20, the membrane was incubated with horseradish peroxidase-conjugated anti-rabbit IgG (Santa Cruz Biotechnology, CA, USA) at room temperature for 40 min. Bound horseradish peroxidase was visualized with enhanced chemiluminescence using Western blotting detection reagents (Amersham Biosciences Corp., Piscataway, NJ, USA) and laser densitometry (Molecular Dynamics, Sunnyvale, CA, USA).

3. Results

3.1. Effects of SOC inhibitors on thapsigargin- and UTP-induced Ca^{2+} responses in A431 cells

In the absence of external Ca^{2+}, thapsigargin induced Ca^{2+} release from internal Ca^{2+} stores by inhibiting endoplasmic reticulum Ca^{2+}-ATPase, and induced capacita-

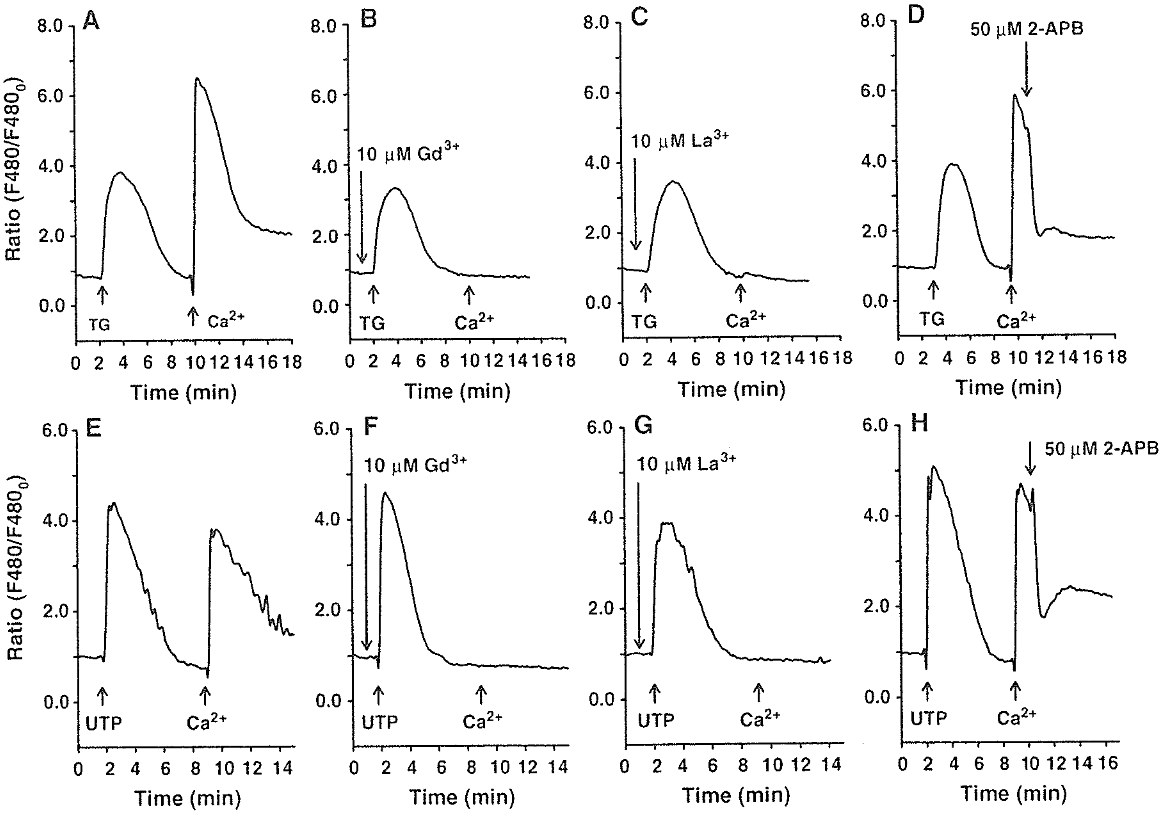

Fig. 1. Effects of trivalent cations and a store-operated Ca^{2+} channel inhibitor on thapsigargin- and UTP-induced Ca^{2+} responses in fluo-3-loaded A431 cells. In the experiment, the medium was changed from HBSS to Ca^{2+}-free HBSS. Test agents were applied as indicated with arrows. After store depletion by thapsigargin (TG, 1 μM, A–D) or UTP (100 μM, E–H), $CaCl_2$ (Ca^{2+}, 2 mM) was added to the medium to initiate capacitative Ca^{2+} entry. Data shown are representative records from at least three experiments. Each trace shown is the mean value of five to seven cells in a field. Ratio ($F480/F480_0$); normalized fluorescent intensity to indicate the changes in $[Ca^{2+}]_i$, where $F480_0$ indicates basal fluorescence.

tive Ca^{2+} entry upon Ca^{2+} addition (Fig. 1A). On the other hand, UTP, a PLC-linked agonist, induced Ca^{2+} release from endoplasmic reticulum in the absence of external Ca^{2+} and then evoked capacitative Ca^{2+} entry upon the addition of external Ca^{2+} (Fig. 1E). Trivalent cations such as Gd^{3+} and La^{3+} (10 μM) completely blocked the capacitative Ca^{2+} entries induced by thapsigargin and UTP, although these cations did not prevent Ca^{2+} release from intracellular Ca^{2+} stores (Fig. 1B, C, F and G). Thapsigargin- and UTP-induced capacitative Ca^{2+} entries into A431 cells were less sensitive to Ni^{2+}, and were inhibited with higher concentrations of Ni^{2+} (>200 μM, data not shown). 2-APB (50 μM), a SOC inhibitor, inhibited capacitative Ca^{2+} entry extremely rapidly when applied after the activation of SOCs with thapsigargin or UTP (Fig. 1D and H). SKF-96365 (25–50 μM), another SOC inhibitor, inhibited the capacitative Ca^{2+} entries induced by both agents, but the potency was modest (data not shown).

3.2. Expression of mRNAs and proteins for TRPC channels

hTRPC1 and hTRPC5 mRNAs were detected in A431 cells, whereas mRNAs for hTRPC1, 3, 4, 5, 6 and 7 were detected in human brain cells as a positive control (Fig. 2A). The human orthologue of the TRPC2 gene, which appears to be a pseudogene, was neither detected in A431 cells nor human brain cells (data not shown). mRNAs for α and β subunits of L-type voltage-dependent Ca^{2+} channels (L-VDCC), marked in human brain cells and NCI-H295 human adrenocortical carcinoma cells (Fig. 2B), were not detected in A431 cells, in accordance with electrophysiological studies revealing the absence of L-VDCC in this cell line (Moolenaar et al., 1986). Western blotting with anti-TRPC1 and TRPC5 antibodies revealed the expression of a protein for TRPC1 and TRPC5 with a molecular weight of around 60 kDa in A431 cells (Fig. 2C, lanes 1 and 3). Bands for TRPC1 and TRPC5 did not appear when antibodies were preincubated with their respective antigens (Fig. 2C, lanes 2 and 4).

4. Discussion

The previous finding that amlodipine, a Ca^{2+} channel blocker, inhibited the growth of A431 cells partly via the attenuation of capacitative Ca^{2+} entry led us to perform experiments to identify the molecular components of SOCs in A431 cells. Mammalian homologs of the *Drosophila* canonical TRPC channel family have been suggested to act as molecular components of SOCs and receptor-activated cation channels in many tissues (Vennekens et al., 2002). In proliferating human pulmonary artery smooth muscle cells, it was shown that TRPC1 and TRPC6 mRNA and protein expressions are upregulated and the amplitude of capacitative Ca^{2+} entry is enhanced (Landsberg and Yuan, 2004). Another study demonstrated that siRNA targeting TRPC4 attenuated ATP-mediated increases in TRPC4 expression, capacitative Ca^{2+} entry amplitude, and ATP-induced proliferation of human pulmonary artery smooth muscle cells (Zhang et al., 2004). Thus,

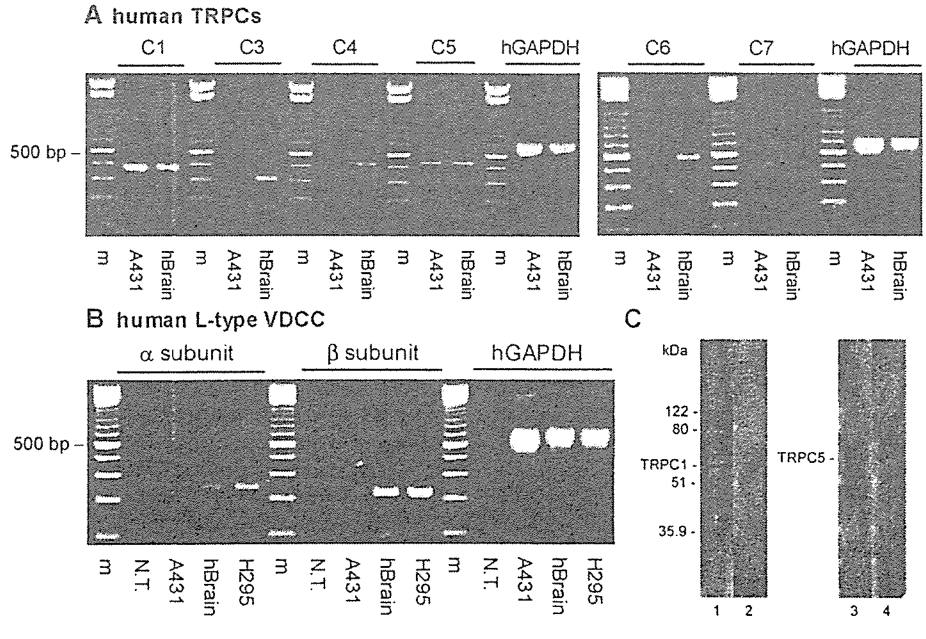

Fig. 2. (A) RT-PCR-amplified products for hTRPC1, hTRPC3–7, and hGAPDH (house keeping gene). hTRPC1 and hTRPC5 mRNAs were detected in A431 cells. All types of hTRPC mRNAs except for that of hTRPC2 were expressed in the human brain (hBrain; Stratagene) as a positive control. (B) RT-PCR-amplified products for α and β subunits of hVDCC. Human brain cDNA (hBrain; Stratagene) and cDNA from human adrenocortical carcinoma cells H295 (H295) were used for positive controls. m; marker, 100 bp ladder. N.T., negative control without template cDNA. (C) Western blots for hTRPC1 and hTRPC5 in A431 cell lysate. The blot was probed with anti-TRPC1 antibody (lane 1), anti-TRPC1 antibody preincubated with the control peptide antigen (lane 2), anti-TRPC5 antibody (lane 3), and anti-TRPC5 antibody preincubated with the control peptide antigen (lane 4).

there is growing evidence to suggest that capacitative Ca^{2+} entry through SOCs is related to cell proliferation in several cell types.

At first, we performed fluorometric Ca^{2+} imaging to elucidate the properties of SOCs in A431 cells in response to store depletion with thapsigargin or UTP. We have already shown that UTP-induced Ca^{2+} responses in A431 cells are mediated via the stimulation of P2 receptors and 1,4,5-triphosphate (IP_3) production by PLC activation, since the responses were inhibited by the putative non-selective P2 receptor antagonist, suramin, and the PLC inhibitor, U73122 (Yoshida et al., 2004). We examined the effects of inorganic inhibitors such as Gd^{3+}, La^{3+}, and Ni^{2+} and organic SOC inhibitors such as 2-APB and SKF-96365 (Clementi and Meldolesi, 1996), on thapsigargin- or UTP-induced Ca^{2+} responses in A431 cells. Both Gd^{3+} and La^{3+}, at concentrations of 10 μM, completely inhibited the capacitative Ca^{2+} entry evoked by thapsigargin or UTP. 2-APB (50 μM), known as an inhibitor of IP_3 receptors and SOC channels (Ma et al., 2000), blocked both agents from inducing capacitative Ca^{2+} entry when applied after the activation of SOCs by Ca^{2+} addition (Fig. 2D and H). Application of 2-APB (>25 μM) itself in Ca^{2+}-free HBSS caused a transient rise in $[Ca^{2+}]_i$ (data not shown), possibly due to its inhibitory action on endoplasmic reticulum Ca^{2+}-ATPase (Bilmen et al., 2002). The above findings clearly indicated the presence of functional SOCs in A431 cells.

To screen human TRPCs (hTRPCs) expressed in A431 cells, we then performed an RT-PCR assay. RT-PCR revealed that mRNAs for hTRPC1 and hTRPC5 are expressed in A431 cells. In Western blot analysis, antibodies to TRPC1 and TRPC5 (Alomone Labs.) detected a protein with an apparent molecular mass of about 60 kDa. This molecular weight is less than the putative molecular masses of 75.9 and 97 kDa for TRPC1 and TRPC5, respectively; however, this band disappeared in both cases following preabsorption with respective specific antigens, suggesting signal specificity. Though the splice variants for human TRPC5 have not been reported, it is possible that A431 cells express a splice variant form of TRPC5. A deletion may occur in the cytoplasmic amino-terminus region encoded by exons 2 and 3, because a PCR-amplified product was undetectable in A431 cells using another set of primers (location of sequence; 879–1785, PCR product; 907 bp) for TRPC5, while a product was detected in the human brain as a positive control (data not shown). It is also possible that the anti-TRPC1 antibody detected a splice variant or truncated form of TRPC1 in A431 cells. Ma et al. (2003), using a mouse polyclonal antibody against the amino-terminus region of hTRPC1, demonstrated that A431 cells express detectable levels of TRPC1 protein. They also suggested that TRPC1 may function as a receptor-operated Ca^{2+} channel through an association with TRPC4 or TRPC5 in the cells after conducting electrophysiological studies (Ma et al., 2003). In this study, we demonstrated the expression of mRNAs and proteins for hTRPC1 and hTRPC5 with functional properties of SOCs in native A431 cells for the first time. Diacylglycerols directly activate hTRPC3 and hTRPC6 (Hofmann et al., 1999) and have no effect on TRPC5 (Venkatachalam et al., 2003). We observed that 1, 2-dioctanoyl-*sn*-glycerol, an analogue of diacylglycerols, did not evoke Ca^{2+} responses in A431 cells (data not shown). This observation appears not to be in conflict with the results from the RT-PCR indicating the mRNA expression of hTRPC5 but not hTRPC3 or hTRPC6 in A431 cells. TRPC1 is widespread and can form heteromultimeric channels with subgroup family members (Vennekens et al., 2002). Indeed, a systematic biochemical study of TRPC interactions in the mammalian brain have shown that TRPC1 forms a heteromer with TRPC4 or TRPC5 (Strübing et al., 2003). It is possible that hTRPC1 is co-expressed with hTRPC5 in heteromultimers and may function as an SOC and/or receptor-activated cation channel in A431 cells. To verify this possibility, gene downregulation studies with antisense oligonucleotides or siRNAs for TRPC1/5 will be needed.

In conclusion, this study revealed that capacitative Ca^{2+} entry in A431 cells in response to store depletion was sensitive to Gd^{3+}, La^{3+} and 2-APB and that A431 cells express mRNAs and proteins for hTRPC1 and C5. These results will be useful to help identify the role of TRPCs in tumor cell proliferation and to clarify mechanism(s) underlying the antiproliferative effect of some dihydropyridine Ca^{2+} channel blockers, such as amlodipine, in A431 cells.

Acknowledgments

We thank Prof. Katsuzo Nishikawa for generously donating the A431 cell line. We also thank Yasuko Shinzawa for secretarial assistance.

References

Bilmen, J.G., Wootton, L.L., Godfrey, R.E., Smart, O.S., Michelangeli, F., 2002. Inhibition of SERCA Ca^{2+} pumps by 2-aminoethoxydiphenyl borate (2-APB). 2-APB reduces both Ca^{2+} binding and phosphoryl transfer from ATP, by interfering with the pathway leading to the Ca^{2+}-binding sites. Eur. J. Biochem. 269, 3678–3687.

Clementi, E., Meldolesi, J., 1996. Pharmacological and functional properties of voltage-independent Ca^{2+} channels. Cell Calcium 19, 269–279.

Hofmann, T., Obukhov, A.G., Schaefer, M., Harteneck, C., Gudermann, T., Schultz, G., 1999. Direct activation of human TRPC6 and TRPC3 channels by diacylglycerol. Nature 397, 259–263.

Landsberg, J.W., Yuan, J.X., 2004. Calcium and TRP channels in pulmonary vascular smooth muscle cell proliferation. News Physiol. Sci. 19, 44–50.

Ma, H.T., Patterson, R.L., van Rossum, D.B., Birnbaumer, L., Mikoshiba, K., Gill, D.L., 2000. Requirement of the inositol trisphosphate receptor for activation of store-operated Ca^{2+} channels. Science 287, 1647–1651.

Ma, R., Rundle, D., Jacks, J., Koch, M., Downs, T., Tsiokas, L., 2003. Inhibitor of myogenic family, a novel suppressor of store-operated currents through an interaction with TRPC1. J. Biol. Chem. 278, 52763–52772.

Moolenaar, W.H., Aerts, R.J., Tertoolen, L.G., De Laat, S.W., 1986. The epidermal growth factor-induced calcium signal in A431 cells. J. Biol. Chem. 261, 279–284.

Putney Jr., J.W., Broad, L.M., Braun, F.J., Lievremont, J.P., Bird, G.S., 2001. Mechanisms of capacitative calcium entry. J. Cell. Sci. 114, 2223–2229.

Strübing, C., Krapivinsky, G., Krapivinsky, L., Clapham, D.E., 2003. Formation of novel TRPC channels by complex subunit interactions in embryonic brain. J. Biol. Chem. 278, 39014–39019.

Venkatachalam, K., Zheng, F., Gill, D.L., 2003. Regulation of canonical transient receptor potential (TRPC) channel function by diacylglycerol and protein kinase C. J. Biol. Chem. 278, 29031–29040.

Vennekens, R., Voets, T., Bindels, R.J., Droogmans, G., Nilius, B., 2002. Current understanding of mammalian TRP homologues. Cell Calcium 31, 253–264.

Yoshida, J., Ishibashi, T., Nishio, M., 2001. Growth-inhibitory effect of a streptococcal antitumor glycoprotein on human epidermoid carcinoma A431 cells: involvement of dephosphorylation of epidermal growth factor receptor. Cancer Res. 61, 6151–6157.

Yoshida, J., Ishibashi, T., Nishio, M., 2003. Antiproliferative effect of Ca^{2+} channel blockers on human epidermoid carcinoma A431 cells. Eur. J. Pharmacol. 472, 23–31.

Yoshida, J., Ishibashi, T., Nishio, M., 2004. Antitumor effects of amlodipine, a Ca^{2+} channel blocker, on human epidermoid carcinoma A431 cells in vitro and in vivo. Eur. J. Pharmacol. 492, 103–112.

Zhang, S., Remillard, C.V., Fantozzi, I., Yuan, J.X., 2004. ATP-induced mitogenesis is mediated by cyclic AMP response element-binding protein-enhanced TRPC4 expression and activity in human pulmonary artery smooth muscle cells. Am. J. Physiol., Cell Physiol. 287, C1192–C1201.

Microvessel Density: Correlation with ^{18}F-FDG Uptake and Prognostic Impact in Lung Adenocarcinomas

JianFei Guo, MD[1,2]; Kotaro Higashi, MD[1]; Yoshimichi Ueda, MD[3]; Manabu Oguchi, MD[1]; Tsutomu Takegami, MD[4]; Hirohisa Toga, MD[5]; Tsutomu Sakuma, MD[6]; Hajime Yokota, MD[1]; Shogo Katsuda, MD[3]; Hisao Tonami, MD[1]; and Itaru Yamamoto, MD[1]

[1]Department of Radiology, Kanazawa Medical University, Ishikawa, Japan; [2]Department of Radiology, First Affiliated Hospital, China Medical University, Shenyang, People's Republic of China; [3]Department of Pathology, Kanazawa Medical University, Ishikawa, Japan; [4]Department of Medical Research Institute, Kanazawa Medical University, Ishikawa, Japan; [5]Division of Respiratory Disease, Department of Internal Medicine, Kanazawa Medical University, Ishikawa, Japan; and [6]Department of Thoracic Surgery, Kanazawa Medical University, Ishikawa, Japan

Although researched for many years, the prognostic value of tumor angiogenesis reflected by microvessel density (MVD) is still controversial, and there have been no previous reports regarding the correlation with ^{18}F-FDG uptake in lung adenocarcinomas. Therefore, in the present study, we investigated the correlation between MVD determined with different endothelial cell antibodies and ^{18}F-FDG uptake and compared the prognostic impact of those factors in lung adenocarcinomas. **Methods:** Forty-four patients with 45 lung adenocarcinomas underwent ^{18}F-FDG PET before surgery. Consecutive paraffin-embedded sections obtained from each resected tumor were immunostained for CD31 (a panendothelial cell marker), CD105 (a proliferation-related endothelial cell marker), and CD34/α-SMA (for double labeling of endothelial cells and mural cells). Four high-power fields in the area with the highest MVD were selected for analysis. Computer-assisted image analysis was used to assess MVD. **Results:** MVD staining results for panendothelial cell markers can be classified into 3 microvessel patterns: diffuse, alveolar, and mixed. The highly ordered alveolar pattern is believed to represent preexisting alveolar vessels trapped in lung adenocarcinomas and may have no significant meaning for the aggressiveness of tumors. Preexisting alveolar cells also do not contribute to ^{18}F-FDG uptake. CD105 staining of MVD (CD105-MVD) showed a significantly positive correlation with ^{18}F-FDG uptake ($P < 0.0001$), whereas CD31 staining of MVD (CD31-MVD) showed a marginally negative correlation with it ($P = 0.057$). Although CD105-MVD correlated negatively with prognosis, patients with low CD105-MVD, compared with those with high or moderate CD105-MVD, had a much better prognosis in both disease-free and overall survival analyses ($P = 0.017$ and $P = 0.013$, respectively). Patients with low CD31-MVD had the worst prognosis ($P = 0.032$ for disease-free survival analysis and $P = 0.179$ for overall survival analysis). **Conclusion:** There is no positive correlation between ^{18}F-FDG uptake and MVD determined with panendothelial cell markers (CD31 and CD34); in contrast, there is a marginally negative correlation between them. MVD determined with CD105, which is a proliferation-related endothelial cell marker, reflects active angiogenesis, correlates positively with ^{18}F-FDG uptake, and is a better indicator of prognosis in lung adenocarcinomas.

Key Words: PET; ^{18}F-FDG; lung cancer; microvessel density; prognosis

J Nucl Med 2006; 47:419–425

Lung cancer is the leading reason for cancer-related deaths in Japan and most Western countries. Surgery is the main method of therapy and also can be combined with radiotherapy and chemotherapy. However, the mortality of lung cancer is still very high; the 5-y survival expectation is only 70%–80%, even in the very early stages (*1,2*). Adenocarcinoma is the most common histologic type of lung cancer and accounts, to a great extent, for the increasing incidence of lung cancer in recent years (*3*). The established prognostic criteria for patients with non–small cell lung carcinoma (NSCLC), such as pathologic stage, can serve as a good indicator of a patient's outcome; however, this staging system does not determine accurately an individual patient's prognosis. Therefore, there is an urgent need to identify and validate new molecular markers and imaging techniques to better identify patients at risk for recurrent disease and metastatic disease, so that patients who might benefit from adjuvant therapy after surgery can be selected.

Tumor angiogenesis is an essential requirement for the development, progression, and metastasis of malignant tumors (*4*). Immunohistochemical staining measurements of angiogenesis with antibodies to factor VIII, CD31, CD34, or CD105 can be used to determine microvessel density (MVD), an important prognostic factor that is independent of other known prognostic variables in several

---

Received Aug. 16, 2005; revision accepted Nov. 30, 2005.

For correspondence or reprints contact: Kotaro Higashi, MD, Department of Radiology, Kanazawa Medical University, 1-1, Daigaku, Uchinada, Kahoku-gun, Ishikawa 920-0293, Japan.
E-mail: h550208@kanazawa-med.ac.jp

cancer types (*5*), including lung cancer (*6–12*). However, whereas some reports have found that MVD is an important prognostic factor in lung cancer (*6,7,10,12*), some reports have failed to do so (*8,9,11*). Therefore, although MVD estimation has promising prognostic prospects, a consensus as to whether MVD is a prognostic marker in lung cancer has yet to be reached.

^{18}F-FDG PET has been applied in many kinds of tumors and is regarded as a good imaging technique for predicting prognosis in some tumors (*13,14*), especially lung cancer (*15–19*). In previous studies, it was demonstrated that ^{18}F-FDG uptake is a significant prognostic factor in patients with NSCLC or adenocarcinoma (*16,19*)—and is even better than pathologic stage (*16*). Furthermore, some studies showed that there is a significant correlation between ^{18}F-FDG uptake and blood flow in breast cancer (*20*). However, although tumor angiogenesis showed a correlation with blood flow, the 2 factors are still quite different from each other. To date, there has been no report regarding the correlation between MVD and ^{18}F-FDG uptake in lung adenocarcinoma. Therefore, in the present study, we investigated not only whether tumor angiogenesis reflected by MVD determined with CD31 or CD105 is a good prognostic factor but also whether there is any correlation between MVD and ^{18}F-FDG uptake in patients with lung adenocarcinoma.

MATERIALS AND METHODS

Patients

Forty-four patients (20 men and 24 women; age range, 47–82 y; mean age, 65 y) with 45 lung adenocarcinomas were included in this study. Twelve patients had bronchioloalveolar carcinoma (BAC), 12 had well-differentiated adenocarcinoma, 14 had moderately differentiated adenocarcinoma, 5 had poorly differentiated adenocarcinoma, and 1 had 2 types of cancer (moderately differentiated adenocarcinoma and poorly differentiated adenocarcinoma). All patients underwent a thoracotomy within 4 wk after their ^{18}F-FDG PET study. No patient had received neoadjuvant chemotherapy or radiotherapy before surgery. Final diagnoses were established histologically (via the thoracotomy) in all patients, and the pathologic stage of each tumor was recorded with the TNM staging system. The sizes of the tumors were determined from the resected specimens and ranged in diameter from 1.2 to 5.5 cm. None of the patients had insulin-dependent diabetes, and the serum glucose levels in all patients just before ^{18}F-FDG injection were less than 120 mg/dL. Informed consent was obtained from all patients participating in this study.

^{18}F-FDG PET Imaging

^{18}F-FDG PET was performed by use of a PET camera (Headtome IV; Shimadzu) with a 10-cm axial field of view. The Headtome IV has 4 detector rings with 768 bismuth germanate crystals per ring. It uses direct and cross-plane coincidence detection to generate 14 slices per bed position. For the thorax, 2 bed positions (28 slices at 6.5-mm intervals) were obtained. Reconstruction in a 128 × 128 matrix with a Hann filter (0.5 cutoff) yielded 5-mm intrinsic resolution at the center. Transmission scans were obtained in all subjects before ^{18}F-FDG administration for attenuation correction with a ^{68}Ge ring source. x-Ray fluoroscopy was used to ascertain the location of the pulmonary nodule, and marks were made on the skin to aid in positioning the patient for the transmission scan. A transmission scan was acquired for 10–20 min in each bed position, depending on the specific radioactivity of the ring sources at the time of the study, for at least 2 million counts per slice. During the transmission scan, marks were made on the patient's skin to aid in repositioning for the emission scan. However, because of the limitation of the available equipment, we could not perform respiratory gating to avoid respiratory motion, which may affect the standardized uptake value (SUV) to some degree. Blood (1 mL) was drawn for baseline blood glucose estimation, and the data were recorded. Immediately after the transmission scan, ^{18}F-FDG was administered intravenously. The average injected dose of ^{18}F-FDG was 185 MBq. After a 40-min uptake period, the patient was repositioned in the scanner. An emission scan was acquired for 10 min in each bed position; the process took a total of 20 min.

For semiquantitative analysis of ^{18}F-FDG uptake, regions of interest (ROIs) were manually defined on the transaxial tomograms that showed the highest uptake to be in the middle of the tumor. The ROIs placed on the lesions encompassed all pixels within lesions that had uptake values of greater than 90% the maximum uptake in that slice, and the average count rate in each ROI was calculated. In patients in whom no nodules were detectable by PET, the ROIs were extrapolated from chest CT scans. After correction for radioactive decay, we analyzed the ROIs by computing the SUVs as follows: PET counts per pixel per second times calibration factor per injected dose (MBq) per kilogram of body weight, where the calibration factor was (MBq/mL)/(counts/pixel/s).

Immunohistochemical Analysis

Immunohistochemical Analysis with a Panendothelial Cell Marker. Monoclonal antibody (mAb) JC70 (Dako), recognizing panendothelial cell antigen CD31 (platelet/endothelial cell adhesion molecule), was used for microvessel staining of 5-μm paraffin-embedded sections. Sections were dewaxed, rehydrated, and microwaved (3 times for 4 min each time) for antigen retrieval. Endogenous peroxidase activity was blocked by incubation in 0.3% hydrogen peroxide in methanol. Nonspecific protein binding was inhibited by treatment with 10% normal serum for 10 min at 37°C. The specimens then were incubated with mAb JC70 overnight at 4°C. The slides were preincubated and rinsed in phosphate-buffered saline and then treated with the biotinylated secondary antibody and peroxidase-conjugated streptavidin. The final reaction product was revealed by exposure to 0.03% diaminobenzidine, and the nuclei were counterstained with Mayer hematoxylin. As a negative control, appropriately diluted nonimmune sera were applied instead of the primary antibody.

Immunohistochemical Analysis with a Proliferation-Related Endothelial Cell Marker. CD105 was stained with mAb SN6 h (1:100; Dako) (*21*) by use of a sensitive immunohistochemical staining system (CSA System; Dako). All of the procedures were performed in accordance with the manufacturer's protocol. Sections were incubated with the anti-CD105 mAb diluted 1:100 for 1 h at room temperature. Normal mouse IgG was used instead of the primary antibody as a negative control.

Double-Labeling Immunohistochemical Technique for CD34 and α-SMA. A double-labeling immunohistochemical technique with a specific double-labeling kit (Envision+ System; Dako) was used to simultaneously stain endothelial cells (CD34) and mural cells (α-SMA) (*22*) to quantitatively assess the pericyte coverage of microvessels. Peroxidase activity was blocked in deparaffinized and rehydrated tissue sections, and the sections were trypsinized, incubated with blocking serum, and then doubly stained for CD34 to label endothelial cells and for α-SMA to detect pericytes and smooth muscle cell expression. For CD34 staining, sections were incubated with a mouse mAb (clone BI-3C5, 1:50 dilution; Zymed) overnight at 4°C. A biotinylated secondary antibody, streptavidin–alkaline phosphatase complex, and diaminobenzidine as a substrate were used to visualize binding of the CD34 antibody. For subsequent staining of α-SMA, sections were incubated with a mouse anti–human α-SMA mAb (clone 1A4, 1:50 dilution; Sigma) for 2 h at room temperature. The color was developed by 20 min of incubation with new fuchsin solution.

Assessment of MVD

Assessment of MVD was performed by computer-assisted image analysis as suggested previously but with some modifications (*23,24*). Vessels with a clearly defined lumen or well-defined linear vessel shape but not single endothelial cells were considered for microvessel assessment. The areas with the highest vascularization were scanned and chosen at low power (×100), and 4 chosen ×200 fields with the highest vascularization were recorded with a digital camera. The captured images were 24 bit and had a resolution of 2,272 × 1,704 pixels. Adobe Photoshop (version 6.0; Adobe Systems Inc.) was used to outline microvessels and convert the images into binary, black-and-white images; the converted images were imported into the image analysis package NIH image 1.62 (http://rsb.info.nih.gov/nih-image/) to calculate the percentage of stained microvessel area corresponding to the total section area. The average MVDs of the 4 selected areas were grouped into 3 grade categories. For CD31 staining of MVD (CD31-MVD), the categories were as follows: low, 0%–4%; moderate, 4%–8%; and high, >8%. For CD105 staining of MVD (CD105-MVD), the categories were as follows: low, 0%–0.8%; moderate, 0.8%–1.6%; and high, >1.6%.

Statistical Methods

All data are reported as the mean ± 1 SD. All statistical analyses were performed with SPSS for Windows (version 12.0; SPSS Inc.). The χ-square test was used to compare the distributions of values across categoric variables. Differences between continuous variables and dichotomous variables were tested by 1-way ANOVA. Overall and disease-free survival probabilities were calculated with the Kaplan–Meier life table method. Differences between survival probabilities were analyzed by the log-rank test. Probability values of less than 0.05 were considered statistically significant.

RESULTS

Vascular Architecture in Lung Adenocarcinomas

On the basis of the immunohistochemical staining results obtained with antibody against CD31, the vascular architecture in lung adenocarcinomas usually can be classified into 3 kinds of patterns: diffuse, alveolar, and mixed. The diffuse pattern is an angiogenic pattern. Normal lung architecture is replaced diffusely. Vessels and stroma are scattered randomly throughout the tumor (Fig. 1A). The alveolar pattern is a nonangiogenic pattern. Tumor cells fill up the alveoli, exploiting the existing alveolar vessels instead of destroying them (Fig. 1B). The mixed pattern consists of both diffuse and alveolar patterns.

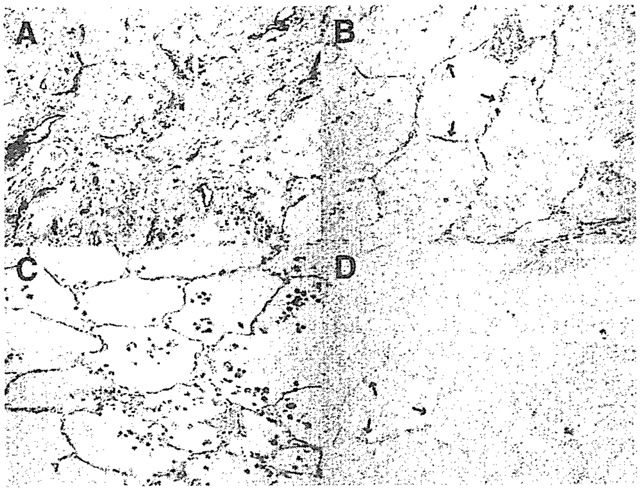

FIGURE 1. (A) Adenocarcinoma with diffuse pattern stained by mAb to CD31. Normal structure was destroyed, and vessels were randomly and diffusely distributed throughout tumor. (B) Adenocarcinoma with alveolar pattern stained by mAb to CD31. Vessels (arrows) in alveolar pattern area were in original distribution; tumor cells filled up alveoli instead of destroying them. (C) Normal alveoli. (D) Consecutive section of same tumor as in B stained by mAb to CD105. Trapped vessels showed negative staining (arrows).

Comparison Between CD34/α-SMA and CD105

For serial sections of lung adenocarcinomas, we compared immunohistochemical staining by mAbs against CD34 (Fig. 2A) and CD105 (Fig. 2B). For CD34 staining, we used a double-labeling technique, staining CD34-positive vessels and vascular pericytes simultaneously. Because the mAb against α-SMA is targeted specifically to pericytes and smooth muscle cells (*22*), vessels with α-SMA expression are mature vessels, and vessels without α-SMA expression are newly formed immature vessels. The total vessel number is usually much higher with CD34 staining and lower with CD105 staining in the same sample; however, as shown in Figure 2, CD34 staining was seen for both mature and immature vessels, whereas CD105 staining was seen mainly for immature vessels. Staining by a mAb against CD31 showed results similar to those for CD34; both mature and immature vessels were stained in the tumors.

Correlation Between MVD and Clinicopathologic Parameters

Table 1 shows the results of a comparison of CD31-MVD and CD105-MVD with clinicopathologic parameters. CD31-MVD showed a correlation with patient age (P = 0.042), sex (P = 0.049), and histologic findings (P = 0.017), whereas CD105-MVD showed a correlation with stage (P = 0.004), tumor size (P = 0.031), and histologic findings (P = 0.007). Our data showed that solitary BAC, a

FIGURE 2. Comparison between CD34/α-SMA double labeling and CD105 in serial sections. (A) Double labeling of CD34 (arrow) and α-SMA (arrowheads). Left vessel was immature vessel showing staining only with CD34. Right vessel was mature vessel showing staining with both CD34 and α-SMA. (B) CD105 staining. Only left, immature vessel was positive for CD105 (arrow). Right, mature vessel was negative for CD105 (double arrows).

subcategory of lung adenocarcinoma with a good prognosis and an MVD that is different from those of other types of adenocarcinoma, had moderate or high CD31-MVD and CD34-MVD but low CD105-MVD.

Correlation Between MVD and ^{18}F-FDG Uptake

Figure 3 shows the correlation of CD31-MVD and CD105-MVD with ^{18}F-FDG uptake. ^{18}F-FDG uptake showed a marginally negative correlation with CD31-MVD ($P = 0.057$), whereas it showed a significantly positive correlation with CD105-MVD ($P < 0.0001$).

Correlation Between MVD and Postoperative Prognosis

Using the Kaplan–Meier method, we analyzed the prognostic impact of CD31-MVD and CD105-MVD in lung adenocarcinomas (Fig. 4). Patients with moderate CD31-MVD had the best disease-free and overall survival probabilities, and patients with low CD31-MVD had the worst prognosis ($P = 0.032$ for disease-free survival analysis and $P = 0.179$ for overall analysis). CD105-MVD correlated negatively with prognosis; patients with low CD105-MVD had the best disease-free and overall survival probabilities ($P = 0.017$ and $P = 0.013$, respectively).

Figures 5 and 6 show 2 representative cases in this study.

DISCUSSION

The present study demonstrated that there is no positive correlation between ^{18}F-FDG uptake and MVD determined with panendothelial cell markers (CD31 and CD34); in contrast, there is a marginally negative correlation between them. Furthermore, MVD determined with CD105, which is a proliferation-related endothelial cell marker, reflects active angiogenesis, correlates positively with ^{18}F-FDG uptake, and is a better indicator of prognosis in lung adenocarcinomas.

Angiogenesis is essential for neoplastic proliferation, progression, invasion, and metastasis because solid tumors cannot grow beyond 1–2 mm in diameter without angiogenesis (*25*). MVD is assumed to reflect the intensity of tumor angiogenesis; indeed, it has been established as a good indicator of prognosis in several cancer types (*5*). However, conflicting results on the prognostic impact of MVD in lung cancer make it difficult to determine the prognostic importance of tumor angiogenesis in lung cancer (*6–12*). Variations in survival results among studies could be explained by the heterogeneity in methodologies used to stain and count microvessels in tumors in addition to variations in patient populations. Differences in reactivity between anti–endothelial cell antibodies used to highlight intratumoral microvessels represent a major bias that should be considered. Although antibodies to CD31 and

TABLE 1
Relationship of Clinicopathologic Parameters to MVD

	CD31-MVD*				CD105-MVD*			
Parameter	Low	Moderate	High	P	Low	Moderate	High	P
Age				0.042				0.254
≤65	10	9	3		11	5	6	
>65	4	9	10		6	8	9	
Sex				0.049				0.376
Male	10	5	6		6	6	9	
Female	4	13	7		11	7	6	
Stage				0.223				0.004
I	11	13	7		16	9	6	
II, III	3	2	5		0	3	7	
Size				0.234				0.031
≤3 cm	8	14	11		16	9	8	
>3 cm	6	4	2		1	4	7	
Histologic findings				0.017				0.007
BAC	0	8	4		9	2	1	
Non-BAC	14	10	9		8	11	14	

*Data are reported as number of tumors.

Non-BAC = well-differentiated adenocarcinoma, moderately differentiated adenocarcinoma, and poorly differentiated adenocarcinoma.

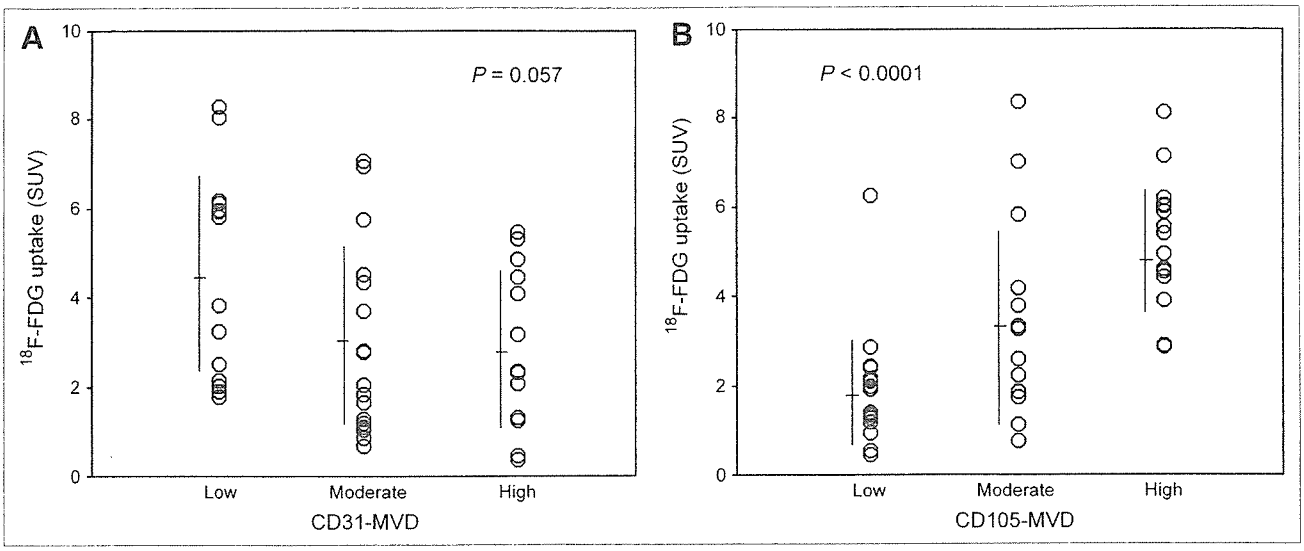

FIGURE 3. (A) CD31-MVD showed negative correlation with ^{18}F-FDG uptake ($P = 0.057$). (B) CD105-MVD showed significantly positive correlation with ^{18}F-FDG uptake ($P < 0.0001$).

CD34 are recommended as standard antibodies for assessing MVD in solid tumors (*26,27*), the variations among studies with these antibodies imply their limitations in lung cancer.

Endothelium in healthy adults is considered quiescent because the turnover of endothelial cells is very low (*28*). However, endothelial cells of tumor-associated neovasculature proliferate 20–2,000 times more rapidly than do endothelial cells of normal tissues (*29*). CD105 (endoglin) is a homodimeric cell membrane glycoprotein expressed on endothelial cells and is thought to be a proliferation-associated marker of endothelial cells (*30,31*). In fact, a correlation has been found between levels of CD105 expression and markers of cell proliferation (i.e., cyclin A and Ki-67) in tumor endothelia (*32*), and some studies have indicated that a greater intensity of staining for CD105 is detectable in blood vessel endothelia within neoplastic tissues than in those within normal tissues (*31,33*). Consistent with these findings, CD105 has been shown to represent an ideal marker for quantifying tumor angiogenesis and to be an independent indicator of prognosis in some tumors (*34,35*), including lung cancer (*21*).

In the present study, by comparing staining results for CD105 and CD34/α-SMA in serial sections of lung adenocarcinomas, we found that CD105 was expressed specifically in immature vessels but not in mature vessels. In areas with an alveolar pattern, we could see clearly the difference between CD31 expression and CD105 expression. The trapped vessels were in the same distribution as in normal alveoli; however, these kinds of vessels were CD31 positive but CD105 negative. Taken together, these findings indicated the following. First, there may be a different mechanism of tumor angiogenesis in lung adenocarcinomas—involving tumor cells filling the alveolar spaces and entrapping, but not destroying, the alveolar septa and co-opting the preexisting blood vessels. Second, because of the presence of the alveolar pattern, comparing the proliferation-related endothelial cell marker CD105 with panendothelial cell markers, such as factor VIII, CD31, and CD34, may not reflect exactly the tumor-associated neovasculature; this may be one of the explanations for the conflicting results regarding MVD studies in lung cancer. Third, although there is a marginally significant correlation between CD31-MVD and prognosis, CD105-MVD has a much more significant prognostic impact than does CD31-MVD; therefore, CD105-MVD is a much better indicator of prognosis in lung adenocarcinomas.

Furthermore, we also found that BAC usually has moderate or high CD31-MVD and CD34-MVD but low CD105-MVD. BAC, as a subcategory of lung adenocarcinoma, has a fairly good prognosis for surgically treated patients. The key pathologic feature of BAC is preservation of the underlying architecture of the lung, with cylindric tumor cells growing on the walls of preexisting alveoli. Therefore, because CD31 and CD34 staining was seen for both mature and immature vessels, it is reasonable to assume that the moderate or high CD31-MVD and CD34-MVD involved mainly preexisting vessels; serial sections stained with CD105 further proved that those vessels were negative for CD105. Although the pathophysiologic impact of preexisting vessels for tumor progression is still unclear, it seems that these kinds of vessels make no contribution to ^{18}F-FDG uptake in lung adenocarcinomas, because most solitary BACs are almost negative in ^{18}F-FDG PET (*36*), even though these BACs have moderate or high CD31-MVD and CD34-MVD.

Regarding the correlation between ^{18}F-FDG uptake and MVD in NSCLC, only 1 previous study mentioned a positive correlation between ^{18}F-FDG uptake and CD34-MVD (*37*). The present study is the first research concentrating

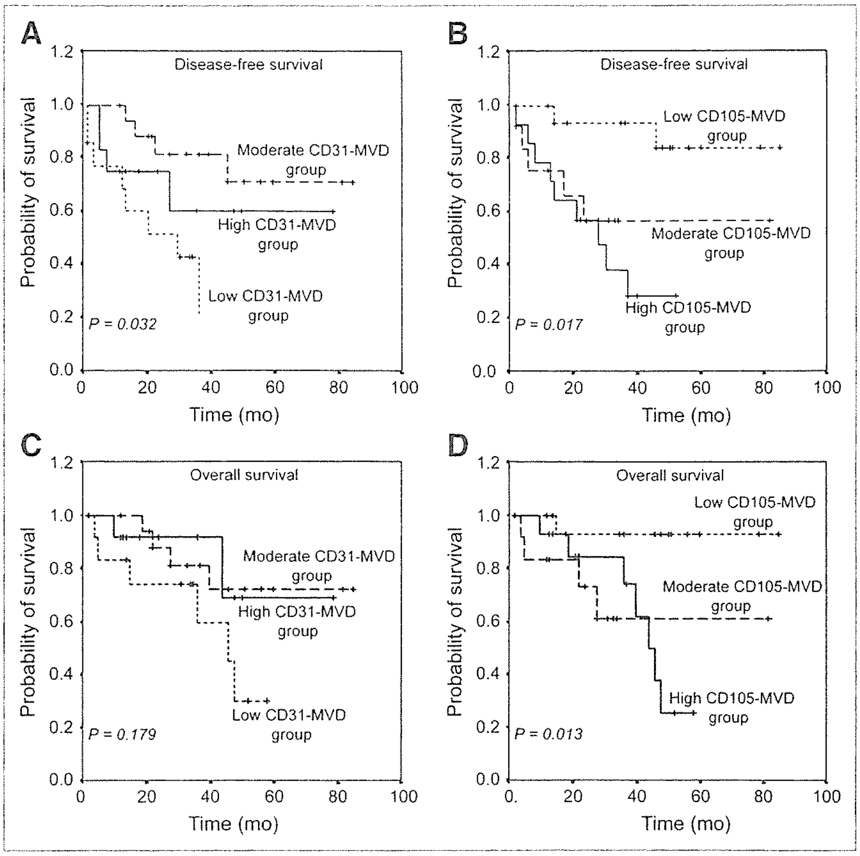

FIGURE 4. Kaplan–Meier survival curves based on MVDs in lung adenocarcinomas. Patients with low CD31-MVD had worst disease-free and overall survival probabilities (A and C), whereas patients with low CD105-MVD had best disease-free and overall survival probabilities (B and D).

on the correlation in lung adenocarcinomas. In contrast to that previous study, our findings suggested that ^{18}F-FDG uptake shows a marginally negative correlation with CD31-MVD but a significantly positive correlation with CD105-MVD. However, the underlying mechanism of this difference is still unclear, and further study is warranted. Although the prognostic impact of MVD in NSCLC is complicated and further study is needed, a new treatment for malignant tumors (antiangiogenic therapy) recently provided new hope for cancer therapy (*38*). Therefore, there is

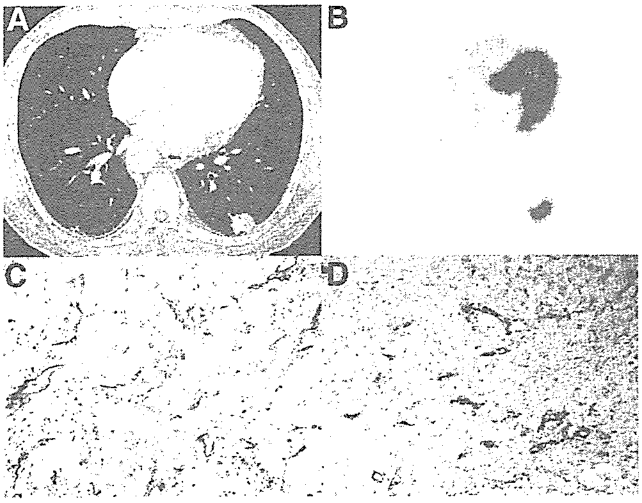

FIGURE 5. Moderately differentiated adenocarcinoma (2.9 cm) with recurrence in 23 mo. (A) CT scan shows nodule in left lung. (B) ^{18}F-FDG PET shows intense uptake of ^{18}F-FDG in tumor (SUV = 5.76). (C) CD31 immunohistochemical analysis shows high MVD. (D) CD105 immunohistochemical analysis also shows high MVD.

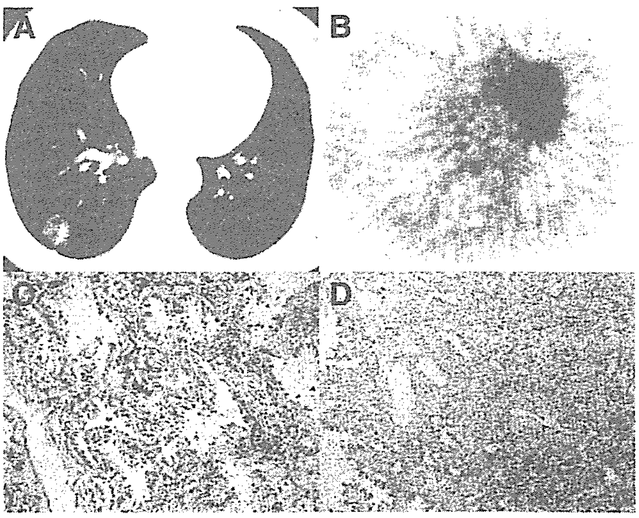

FIGURE 6. BAC (2.0 cm) without recurrence in 50 mo. (A) CT scan shows nodule in right lung. (B) ^{18}F-FDG PET shows modest uptake of ^{18}F-FDG in tumor (SUV = 1.32). (C) CD31 immunohistochemical analysis shows moderate MVD. (D) CD105 immunohistochemical analysis shows low MVD.